minerals

MDPI

Article

Mineralogical Features of Ultramafic and Mafic Rocks of Syum-Keu Ophiolite (Polar Urals, Russia): Implications for Petrology and Paleogeodynamics

Timur D. Shabutdinov, Dmitry E. Saveliev *, Ruslan A. Gataullin and Aidar A. Samigullin

Institute of Geology UFRC RAS, Karl Marks Str., 16/2, 450077 Ufa, Russia; timurgeolog11@gmail.com (T.D.S.); rusgatln97@gmail.com (R.A.G.); samigullinaidar85@gmail.com (A.A.S.)
* Correspondence: savl71@mail.ru

Abstract: The Syum-Keu massif is the northernmost ophiolite complex of the Ural mobile belt. It differs from other massifs of the Polar Urals due to the prominent distribution of lherzolites in the upper mantle section. This feature aligns it more closely to some massifs in the southern part of the belt (Kraka). Thus, a comparison of the ultramafic rock compositions in these massifs is highly relevant. Thus, comparing the compositions of ultramafic rocks from these massifs is highly relevant and is one of the primary objectives of this study. Our second objective is to study the microstructural features of ultramafic rocks from the upper mantle, as they can indicate modes of subsolidus processes that played a key role in the formation of this massif. Our study utilizes optical microscopy, assessments of bulk rock composition using X-ray fluorescence and ICP-MS, as well as mineralogical methods, such as scanning electron microscopy with energy dispersive spectroscopy and electron backscattered diffraction, for the microstructural analysis of peridotites. In addition to ultramafic rocks from the upper mantle section, the composition and mineralogy of mafic rocks from the crustal section were studied. The microstructural analysis of ultramafic rocks indicates their two-stage evolution. The first is associated with plastic flow under the upper mantle conditions dominated by the olivine slip along the {0kl}[100] system, while the second reflects formation in the lower crust, with lower-temperature deformation along the {110}[001] slip system. Comparing the mineralogy of the Syum-Keu peridotites to lherzolite massifs in the Southern Urals reveals a significant difference in accessory Cr-spinel composition; the former show elevated iron content (Fe trend), indicating intense crustal metamorphism. Similarly, amphiboles in Syum-Keu ultramafic rocks exhibit a significant crustal (metamorphic) component, while the same minerals in the Kraka massif suggest a mantle (magmatic) origin. Mafic rocks in the Syum-Keu massif also typically display a high degree of metamorphism. The obtained results generally corroborate prior findings on a longer evolution of the upper mantle ultramafic rocks of the Syum-Keu massif compared to those of the Kraka massif. Our results are also consistent with the suprasubduction nature of these ultramafic rocks. Our findings can be utilized in further studies of the microstructure and composition of ophiolites from the Polar Urals to provide a more detailed characterization of the partial melting conditions of the mantle source, the plastic flow of peridotites, and their interaction with melts and fluids.

Keywords: ultramafic rock; ophiolite; gabbro; peridotite; olivine fabric; Cr-spinel; Syum-Keu; Urals

check for updates

Citation: Shabutdinov, T.D.; Saveliev, D.E.; Gataullin, R.A.; Samigullin, A.A. Mineralogical Features of Ultramafic and Mafic Rocks of Syum-Keu Ophiolite (Polar Urals, Russia): Implications for Petrology and Paleogeodynamics. *Minerals* **2024**, *14*, 1245. https://doi.org/10.3390/min14121245

Academic Editor: Ruibao Li

Received: 2 November 2024
Revised: 2 December 2024
Accepted: 4 December 2024
Published: 6 December 2024

Copyright: © 2024 by the authors. Licensee MDPI, Basel, Switzerland. This article is an open access article distributed under the terms and conditions of the Creative Commons Attribution (CC BY) license (https://creativecommons.org/licenses/by/4.0/).

1. Introduction

Ophiolite associations are widespread in fold belts worldwide and represent fragments of the ancient oceanic crust and upper mantle [1,2]. Typically, these complexes are divided into three main sections, i.e., a lower mantle section, a mantle–crust transitional zone (MTZ) primarily composed of pyroxenites, and an overlying crustal section containing gabbroids, dolerite dikes, and pillow lavas. During the uplift, mantle ultramafic rocks from the upper mantle underwent solid-phase transformations and partial melting. Analyzing the composition and structural features of ultramafic rocks provides valuable insights

into the mechanisms of plastic flow in upper mantle sources and allows for modeling the conditions (P-T-fO_2) that led to the formation of ultramafic rocks as mantle diapirs rose through a spreading zone. Mineralogical and geochemical features of ophiolite rocks are critical for identifying the pressure–temperature (P–T) formation conditions of geological sections and for performing geodynamic reconstructions [3–9].

The mineralogical and structural features of ophiolites indicate a complex evolutionary history, involving deformation, metamorphism, and mantle–crust interactions. The study of other ophiolite complexes has emphasized the role of accessory minerals, such as Cr-spinel, amphiboles and pyroxenes, in reconstructing tectonic settings and mantle processes [8,10–12].

Some techniques, including EBSD and geothermobarometry, have been applied to analyze mantle peridotites and mafic crustal rocks, providing important insights into the mechanisms of the plastic flow in the upper mantle and enabling modeling of the P-T-fO_2 conditions during the massif evolution. Some recent studies have engaged EBSD to analyze chromite and olivine microstructures, revealing crystallographic preferred orientations and deformation mechanisms. These studies contribute to a deeper understanding of deformation mechanisms in ultramafic rocks and emphasize the tectonic evolution and formation of chromitites in response to melt–peridotite interactions [13–15].

2. Geological Background

Structurally, the Syum-Keu massif lies in the Main Ural Fault (MUF) zone in the Polar Urals, displaying an irregular crescent shape on maps, curving westwards (Figure 1). The massif spans an area of approximately 600 km^2 (40–60 km long and up to 12 km wide) [16].

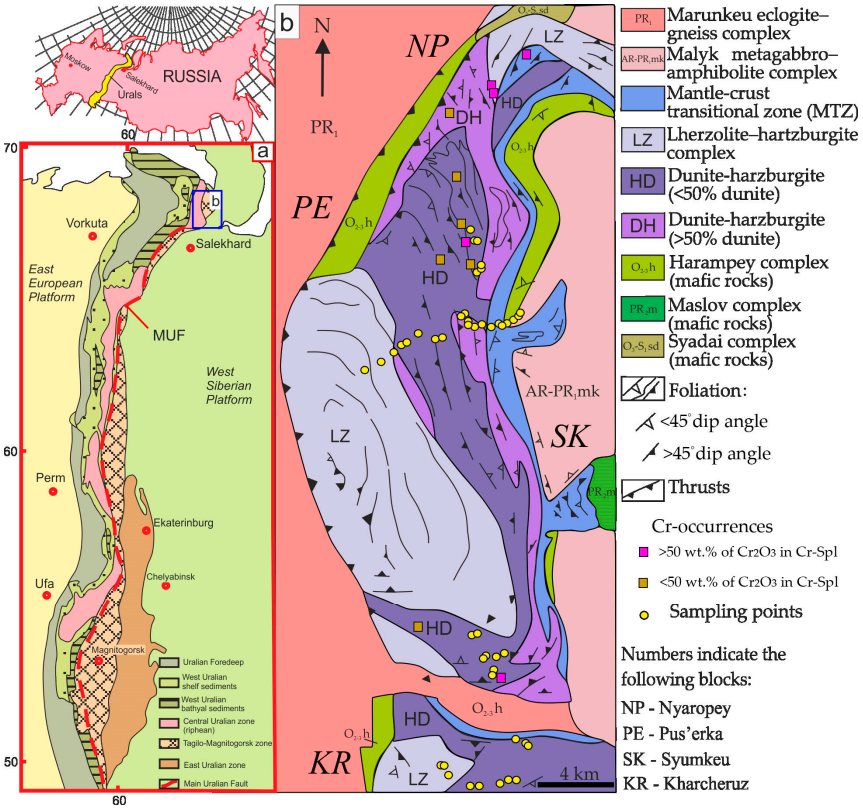

Figure 1. Schematic geological map of the Syum–Keu massif (after [16–19]). (**a**) Schematic map of Urals. (**b**) Geological map of Syum-Keu massif.

Geological study of the Syum-Keu massif began in the 1930s, when ultramafic rocks, gabbros, amphibolites, plagiogranites, and diorites in the MUF zone were classified as part of a single igneous dunite–gabbro–plagiogranite formation. In the 1970s, mafic-ultramafic massifs were reclassified as parts of allochthonous sheets thrust over the Paleozoic for-

mations along the western slope of the Urals. A geological survey was conducted from the 1960s to the 1980s by Yu.N. Nikitin, V.N. Okhotnikov, and A.K. Afanasyev at scales of 1:200,000 and 1:50,000. The survey revealed numerous sites of chromite mineralization [20]. Later on, various researchers examined the structure and material composition of the ultramafic rocks of the Syum-Keu massif [16,18,20–24].

The Syum-Keu massif comprises five main blocks, Shchuch'ya, Nyaropey, Pus'erka, Syum-Keu, and Kharcheruz, with some researchers additionally recognizing the sixth block, Yarkeu [16,22]. Located within the MUF zone, the Syum-Keu massif borders the Marunkeu eclogite-gneiss complex to the west along a thrust zone [17], while to the east, it is constrained by gabbroids of the Malyk, Maslov, and Kharampei complexes within the Shchuchya synclinorium [20]. Within the massif structure, distinct lithological units can be identified, including lherzolite–harzburgite, dunite–harzburgite, and dunite–werlite-clinopyroxenite ("banded") rock complexes [16].

The lherzolite–harzburgite complex comprises harzburgites and diopside harzburgites (60%–80%), with and lherzolites making up 20%–40% of the composition. In the western part of the massif, these rocks exhibit a massive structure with a medium- to coarse-grained texture. In contrast to the lherzolite–harzburgite complex, the dunite-harzburgite one shows a higher dunite content and a medium- to fine-grained texture. The rocks are distributed symmetrically, i.e., harzburgites occur at the margins of the complex, while dunite–harzburgites occupy its central part. The banded complex is traced along the eastern margin of the massif. It is directly adjacent to gabbroids of the Kharampei, Malyk, and Maslov complexes [16]. Studies [16,23] show that the ultramafic section comprises upper mantle tectonites with intense folding that result from the viscous-plastic flow of the material.

Chromitites are major mineral resources known in the massif. They produce small ore bodies of a characteristic podiform type. All of them were found in the 1970–1990s. According to the latest review by [25], the massif hosts 11 ore occurrences with ore reserves of a few to several hundred thousand tons, and a dozen mineralization sites (Figure 1). The composition of chromite grains indicates that some of the ore occurrences belong to the metallurgical type (high-Cr), while the others are of the refractory type (high-Al). The Nyarope ore occurrence is considered the largest, lying in marginal dunites near the boundary between the mantle section and the mantle–crust transitional zone. The mineralization is represented by a series of lenticular bodies of a fine-grained banded and spotted structure, forming an ore zone up to 60 m wide and 300 m long. Chromite grains are characterized by a high-Cr composition.

3. Materials and Methods

3.1. Materials

Ultramafic and mafic rocks for this study were sampled from outcrops in the Syum-Keu massif during fieldworks in 2023. A total of 65 samples were collected from the Pus'erka, Syum-Keu, and Kharcheruz blocks (Figure 1). Most of the samples were selected from outcrops, although some dunite and chromitite specimens were taken from preserved drill cores.

3.2. Methods of Study

The bulk composition of rocks was analyzed for petrogenic oxides and some minor elements using a Xenemetrix X-Calibur X-ray (Migdal Haemek, Israel) fluorescence energy-dispersive spectrometer (Institute of Geology, Ufa Federal Research Center, Russian Academy of Sciences, Ufa). Electron microscopy and mineral composition analyses were performed on polished sections using a Tescan Vega 4 Compact (Brno, Czech Republic) scanning electron microscope equipped with an Oxford Instruments Xplorer (Abingdon-on-Thames, UK) energy-dispersive analyzer (Institute of Geology, Ufa Federal Research Center, Russian Academy of Sciences, Ufa). The spectra were automatically processed with the AzTec 5.1 software package (Oxford Instruments, High Wycombe, UK). The following settings were used for shooting: accelerating voltage of 20 kV, probe current of 3–4 nA, and a spectrum acquision time of 60 s per point in the Point&ID mode.

Mineral formulas were calculated as follows: Cr-spinel and olivine for 4 oxygen atoms, pyroxenes for 6, plagioclase for 8, and garnet for 12. For Cr-spinel, the atoms of divalent and trivalent iron were determined based on the mineral stoichiometry. Amphibole compositions were calculated using a 23-oxygen atom model with the method described in [26]. Chlorite compositions were calculated based on a 28-oxygen atom model. End-member compositions in olivine and pyroxenes were determined as follows: forsterite (Fo = Mg/(Mg + Fe), Atomic Percent (at.%)), enstatite (En = Mg/(Mg + Fe + Ca), at.%), ferrosilite (Fs = Fe/(Mg + Fe + Ca), at.%), and wollastonite (Wo = Ca/(Mg + Fe + Ca), at.%). Mineral abbreviations in figures are provided according to [27]. Alternatively, the minerals are represented by chemical formulas approximating their composition.

Microstructural analyses of ultramafic rocks were performed using electron backscatter diffraction (EBSD). The samples were meticulously polished on diamond pastes followed by mechanochemical polishing with a 0.04 μm colloidal silica suspension (Non-Stick/Rinsable, Allied High Tech Products Inc., Cerritos, CA, USA) to remove work hardening. The analyses were conducted on a Vega Mira SEM (Brno, Czech Republic) at the Collective Use Center "Structural and Physical-Mechanical Methods of Materials Study" at the Institute for Superplasticity Problems of Metals of the Russian Academy of Sciences, Ufa. Primary data were processed using the HKL Channel 5 (Oxford Instruments, High Wycombe, UK) software package and the MTEX program.

4. Results

4.1. Petrography of Ultramafic and Mafic Rocks

Examination of thin sections revealed that peridotites are primarily composed of harzburgites with a lesser proportion of lherzolites, while dunites and pyroxenites were relatively rare (Figure 2). All of the ultramafic rocks studied display varying degrees of serpentinization and more intense metamorphic alterations (Figure 2).

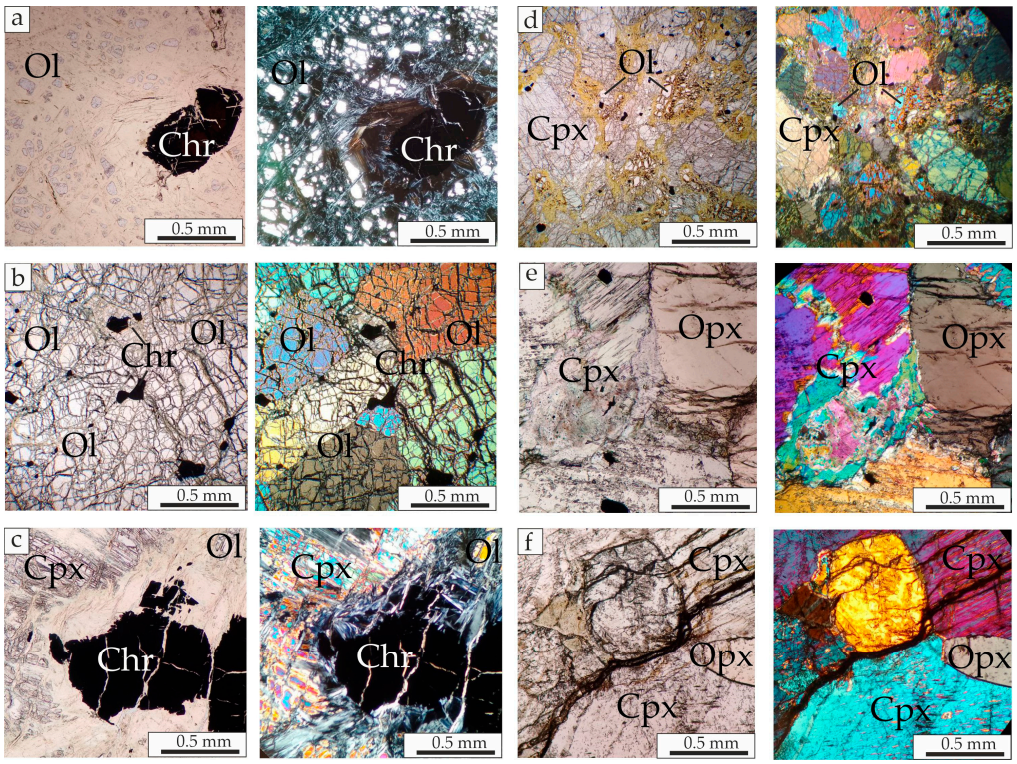

Figure 2. Petrographic features of ultramafic rocks. Transmitted light, in pairs of pictures, with analyzer (right) and without analyzer (left). (**a**,**b**) dunite (S-301-2; S-324); (**c**) lherzolite (S-304-9); (**d**) olivine websterite (S-323-1); (**e**) clinopyroxenite (S-302-3b); (**f**) orthopyroxenite (S-311-4); Cpx—clinopyroxene, Ol—olivine, Opx—orthopyroxene, Chr—Cr–spinels.

In these ultramafic rocks, mesh-textured serpentinization, which is widespread in the Southern Urals massifs, is fairly rare, while antigorite formation is far more prevalent. According to [22], rocks from the central part of the massif were subject to regressive metamorphism of greenschist (α-lizardite+brusite+magnesite) and epidote–amphibolite facies (olivine-early antigorite-α-lizardite+brusite+magnesite-chlorite). In the periphery, a mineral association of β-lizardite+brusite+magnetite is observed, which is compatible to the muscovite–hornblende facies of the contact metamorphism.

Mafic rocks are represented by gabbro–norite, amphibole, and garnet gabbro (Figure 3). The primary rock-forming minerals in these mafic rocks include plagioclase (anorthite ($An_{90–100}$)), orthorhombic and monoclinic pyroxenes, and occasionally garnet. Secondary minerals include amphibole and chlorite (Figure 3). The rocks underwent metamorphism within the garnet–amphibolite and granulite facies [21].



Figure 3. Petrographic features of mafic rocks. Transmitted light, in pairs of pictures, with analyzer (left) and without analyzer (right). (**a**,**b**) Garnet–gabbro (S-314; S-318–1); (**c**,**d**) gabbro–norite (S-316; S-318); (**e**,**f**) amp–gabbro (S-341; S-345). Amp—amphiboles, Chl—chlorite, Cpx—clinopyroxene, Grt—garnet, Opx—orthopyroxene.

4.2. Bulk Compositions of Rocks

4.2.1. Ultramafic Rocks

We recalculated the chemical analyses to determine anhydrous composition and also determined the normative mineral composition, which generally corresponds to harzburgite with clinopyroxene (diopside) content ranging from 3.5% to 4.0%. The main components of the rocks are MgO, SiO_2, and FeO, with a low TiO_2 content (0.1–0.2 Weight Percent (wt.%)). Among the other petrogenic oxides, significant amounts were obtained for CaO (0.8–1.2 wt.%) and Al_2O_3 (1.5–4.0 wt.%). Chemically, these rocks resemble formations from the depleted mantle, such as harzburgites and, less frequently, dunite-harzburgites and dunites (Figure 4a; Table 1). Notably, sample S-304-9 stands out among the studied samples. According to the ternary diagram of the normative mineral composition, it is classified as lherzolite. Most pyroxenites belong to olivine websterites and clinopyroxenites. Chemical analyses were also provided to construct a classification diagram based on the A and S coefficients (Figure 4b).

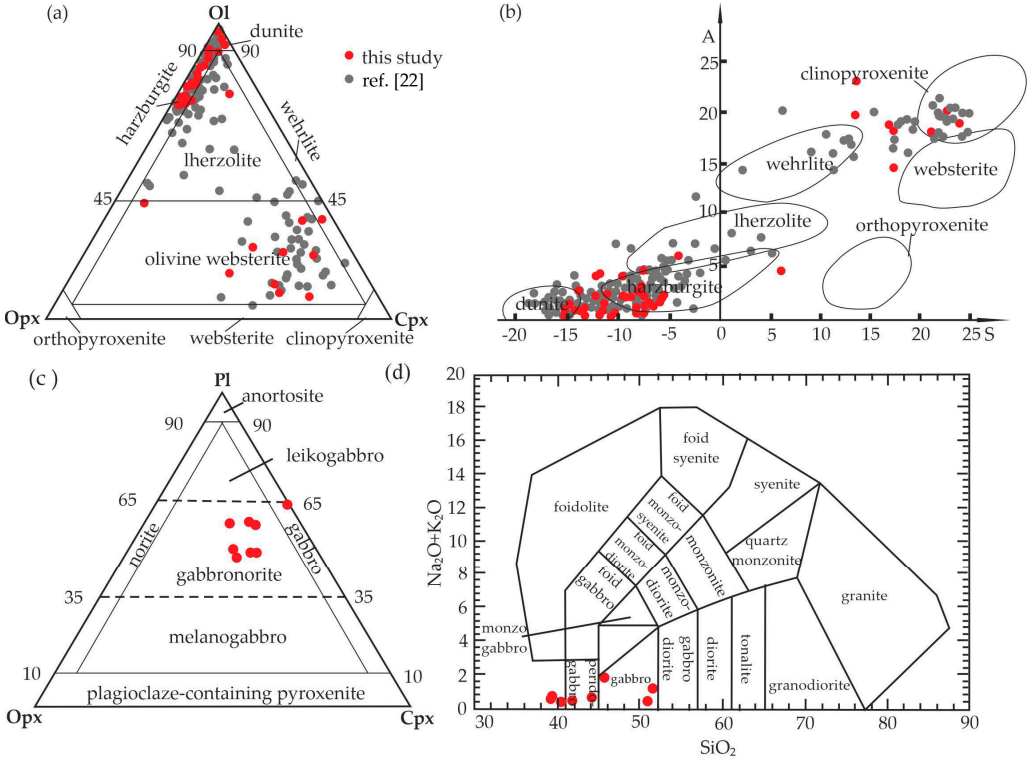

Figure 4. Compositional features of ultramafic and mafic rocks. (**a**) Normative mineral composition ultramafic rocks (peridotites, dunite, pyroxenites), this study and fer. [22]. (**b**) A vs. S diagram, following [28]: A = Al_2O_3 + CaO + Na_2O + K_2O, S = SiO_2 − (Fe_2O_3 + FeO + MgO + MnO + TiO_2). (**c**) Normative mineral composition mafic rocks. (**d**) Total Alkali-Silica (TAS) diagram (SiO_2 vs Na_2O + K_2O), following [29]. Cpx—clinopyroxene, Ol—olivine, Opx—orthopyroxene, Pl—plagioclase.

Table 1. Bulk rock composition of the Syum–Keu ultramafic rocks (wt.%).

wt.%	S-301-2	S-302-1	S-304-9	S-328	S-335-3	S-346-2	S-337-1	S-351D	S-340-3
SiO_2	38.0	39.6	40.0	40.0	36.7	40.1	41.4	31.4	35.2
TiO_2	0.03	0.03	0.05	0.04	0.04	0.05	0.05	0.2	0.05
Al_2O_3	1.8	1.8	1.8	1.4	1.9	0.6	1.1	3.8	1.6
Fe_2O_3	6.4	5.0	4.0	5.8	8.7	12.0	8.4	9.8	8.2
FeO	4.6	3.6	4.5	4.9					
CaO	1.0	1.0	4.6	1.1	1.1	0.2	1.5	0.6	0.1
MgO	38.0	38.5	35.4	37.9	41.8	42.0	38.4	24.8	34.2
MnO	bdl	bdl	bdl	bdl	0.1	0.2	0.1	0.2	0.2
K_2O	0.01	0.01	0.02	bdl	bdl	bdl	bdl	bdl	bdl
Na_2O	0.02	0.06	0.08	0.09	0.16	0.09	0.05	0.05	0.02
LOI	10.3	10.0	9.8	8.1	9.7	3.5	8.2	4.5	12.1
Total	100.2	99.7	100.4	99.4	100.2	98.7	99.3	100.9	91.6
S	−11.1	−7.6	−4.1	−8.7	−13.9	−14.1	−5.5	−3.6	−7.4
A	2.8	2.9	6.5	2.6	3.2	0.9	2.6	4.4	1.8

bdl—below detection limit.

4.2.2. Mafic Rocks

We similarly recalculated the chemical analyses of the gabbroids for their anhydrous composition and also determined their normative mineral composition. The compositions

of the mafic rocks were calculated using a specialized CIPW-calculator developed by the Geology Department in New York, USA (see Supplementary Materials). In most of the studied samples, they correspond to gabbro-norite (Figure 4c; Table 2). The primary components of these rocks include CaO, MgO, FeO, Fe_2O_3, SiO_2, and Al_2O_3. The rocks are low in TiO_2 (0.3–1.0 wt.%) and Na_2O (0.49–1.76 wt.%). Among all of the samples studied, S-331 stands out, as it is classified as gabbro according to the ternary diagram of the normative mineral composition (Figure 4c). On the TAS diagram, the gabbroids plot within the fields designated for gabbro and transitional (gabbro–peridotite) rocks (Figure 4d).

Table 2. Bulk rock composition of the Syum–Keu mafic rocks (wt.%).

wt.%	S-313-2	S-314	S-318-1	S-331	S-347-2	S-348	S-349	S-356
SiO_2	51.0	39.3	42.0	41.0	52.0	45.7	39.5	44.2
TiO_2	0.8	0.8	0.9	0.3	1.0	0.6	0.6	0.4
Al_2O_3	13.0	14.9	16.3	19.0	11.4	13.6	12.1	13.1
Fe_2O_3	5.0	20.6	7.5	5.0	5.6	15.6	23.0	10.4
FeO	7.5	bdl	5.3	2.8	5.0			
MnO	0.03	0.2	0.14	0.08	0.29	0.2	0.2	0.2
MgO	9.0	8.0	10.0	8.4	9.0	8.9	11.2	13.2
CaO	12.7	14.0	14.2	18.9	11.4	10.9	11.8	14.6
Na_2O	0.5	0.7	0.6	0.5	1.3	1.8	0.8	0.8
K_2O	bdl	bdl	bdl	bdl	bdl	0.2	bdl	bdl
P_2O_5	0.10	0.04	0.09	1.01	0.09	0.18	0.09	0.48
LOI	0.5	1.0	2.5	3.2	3.6	2.8	1.3	2.2
Total	99.9	99.6	99.3	99.0	100.3	100.6	100.7	99.6

bdl—below detection limit.

4.3. Mineralogy of Ultramafic Rocks

The rock-forming minerals in ultramafic rocks primarily include olivine, orthopyroxene, and clinopyroxene. Olivine occurs as relics ranging from 0.05 to 0.4 mm in size among mesh-textured serpentine. It shows high Mg content, which increases from harzburgites and lherzolites (Fo_{88} and Fo_{89}, respectively) to dunites (Fo_{94}) (Table 3 and Table S1). The NiO content in olivine varies from 0.27 to 0.39 at.%, gradually rising toward lherzolites.

Table 3. Representative analyses of olivine grains from ultramafic rocks of the Syum-Keu massif.

wt.%	1	2	3	4	5	6	7	8
SiO_2	41.0	41.2	41.0	40.5	41.4	40.6	40.8	40.6
MgO	51.0	52.2	49.3	50.4	53.5	50.3	51.2	50.2
FeO	9.3	7.0	10.7	9.0	5.4	8.9	8.1	9.0
NiO	0.3	0.3	0.3	0.3	0.3	0.4	0.4	0.4
MnO	0.2	0.2	0.2	0.2	0.1	0.1	0.1	0.1
Total	101.8	100.9	101.5	100.4	100.7	100.3	100.6	100.3
apfu								
Mg	1.82	1.86	1.79	1.82	1.90	1.82	1.84	1.82
Fe	0.19	0.14	0.22	0.18	0.11	0.18	0.16	0.18

Table 3. *Cont.*

wt.%	1	2	3	4	5	6	7	8
Ni	0.006	0.005	0.006	0.005	0.006	0.007	0.008	0.008
Mn	0.004	0.004	0.005	0.005	0.001	0.002	0.003	0.002
Si	0.98	0.99	0.98	0.98	0.99	0.99	0.98	0.99
Fo	0.90	0.93	0.89	0.90	0.94	0.91	0.91	0.90

1–5—dunite, 6–8—harzburgite and lherzolite; Fo = Mg/(Mg + Fe).

Pyroxenes are represented by xenomorphic grains ranging from 0.4 to 2.4 mm in size, often with bastite pseudomorphs along their edges. The diagram (Figure 5a; Table 4 and Table S2) shows the compositions of the pyroxenes, with orthopyroxene represented by enstatite and clinopyroxene primarily by diopside and occasionally by low-iron augite.

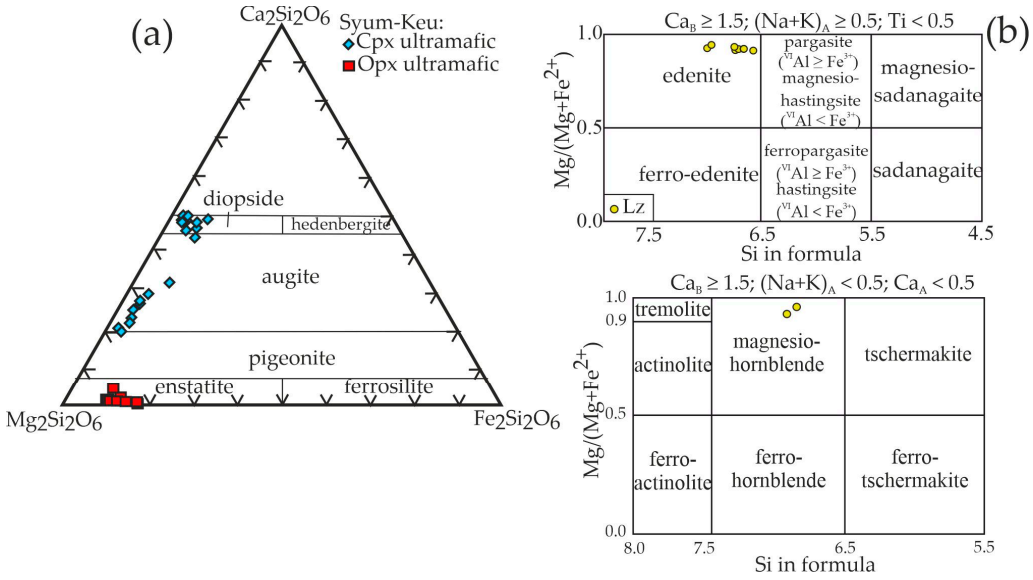

Figure 5. Compositional features of ultramafic rock-forming minerals: (**a**) pyroxenes; (**b**) amphiboles, following [26]; Cpx—clinopyroxenes, Opx—orthopyroxenes, Lz—lherzolites.

Table 4. Representative analyses of pyroxenes from ultramafic rocks of the Syum-Keu massif.

wt.%	1	2	3	4	5
SiO_2	53.65	52.8	55.9	51.7	53.7
MgO	18.84	17.4	23.3	16.0	33.7
CaO	22.75	24.4	17.0	24.3	0.5
Al_2O_3	1.70	2.4	0.8	2.7	2.2
FeO	1.66	2.1	2.0	4.2	6.7
Cr_2O_3	0.52	0.7	0.4	bdl	0.4
TiO_2	bdl	bdl	bdl	0.2	bdl
Na_2O	0.41	0.1	0.4	0.2	bdl
MnO	bdl	bdl	0.1	0.1	0.2
Total	99.53	99.9	99.9	99.4	97.4
apfu					
Na	0.029	0.003	0.030	0.009	–
Mg	1.01	0.94	1.16	0.88	1.78

Table 4. *Cont.*

wt.%	1	2	3	4	5
Ca	0.88	0.95	0.66	0.96	0.02
Al(VI)	0.07	0.10	0.04	0.12	0.09
Ti	–	–	0.001	0.005	–
Cr	0.015	0.019	0.011	–	0.011
Mn	–	–	0.002	0.004	0.006
Fe	0.05	0.06	0.06	0.13	0.20
Si	1.94	1.92	2.03	1.90	1.89
En	0.52	0.48	0.62	0.45	0.89
Wo	0.45	0.49	0.35	0.49	0.01
Fs	0.03	0.03	0.03	0.06	0.10

1–4—clinopyroxene, 5—orthopyroxene; 1—lherzolite, 2, 5—harzburgite, 3—orthopyroxenite, 4—clinopyroxenite; bdl—below detection limit; En = Mg/(Mg + Ca + Fe); Fs = Fe/(Mg + Ca + Fe); Wo = Ca/(Mg + Ca + Fe).

Pyroxenes exhibit elevated Al_2O_3 content, increasing from peridotites (1.7–2.17 at.%) to pyroxenites (2.54–2.69 at.%) and gabbros (3.11 at.%). In addition to primary rock-forming minerals, amphiboles were identified in the samples and were classified as magnesian hornblende ($Ca_2[Mg_4(Al,Fe^{3+})]Si_7AlO_{22}(OH)_2$) and edenite ($NaCa_2Mg_5Si_7AlO_{22}OH)_2$) (Figure 5b; Table S3) [26].

Cr-spinel ($(Mg, Fe^{2+})(Cr, Al, Fe^{3+})_2O_4$) is a consistent accessory mineral found in ultramafic rocks. Additionally, we discovered small grains of pentlandite ($(NiFe)_9S_8$) (10–100 μm), maucherite ($Ni_{11}As_8$) (20–25 μm), millerite (NiS) (45–50 μm), chalcopyrite ($CuFeS_2$) (1–2 μm), cadmium-containing sphalerite ((Zn,Cd)S)) (5 μm), native copper (7–15 μm), potarite (PdHg) (2–3 μm), irarsite ((Ir,Ru,Rh,Pt)AsS) (3 μm), and native osmium (3–4 μm) in the ultramafic rocks and chromitites of the massif (Figure 6). The composition of platinum group minerals (Table S4) depends on their association, i.e., disulfides of the laurite-erlichmanite series commonly occur within an ore's chromite grains, while sulfoarsenides with prevalent iridium (irarsite) are often found in the interstices between chromite grains and their periphery. As for such rare minerals as potarite, they are typically associated with nickel and copper sulfides.

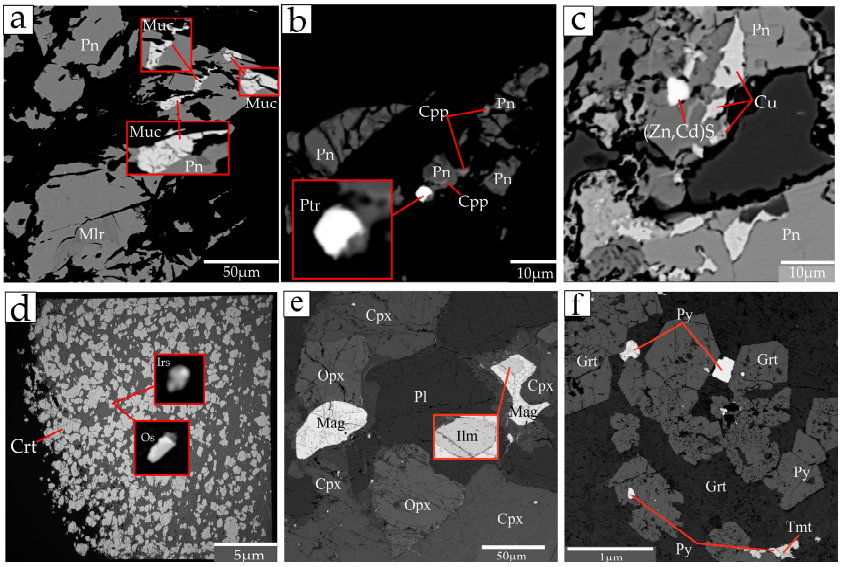

Figure 6. Accessory minerals in (**a**,**d**) dunites (S-348-1A, S-304-1A, S-301-2, S-351D), (**b**) harzburgites (S-328), (**c**) lherzolites (S-337-1), (**e**) gabbro–norites (S-313-2), and (**f**) garnet-bearing gabbro (S-314).

Cpp—chalcopyrite, Cpx—clinopyroxene, Cu—native copper, Grt—garnet, Ilm—ilmenite, Irs—irarsite, Mag—magnetite, Mlr—millerite, Muc—maucherite, Opx—ortopyroxene, Os—native osmium, Pl—plagioclase, Pn—pentlandite, Ptr—potarite, Py—pyrite, Tmt—titanomagnetite, (Zn,Cd)S)—cadmium-bearing sphalerite.

The morphology of accessory Cr-spinel grains varies from anhedral in peridotites to subhedral and euhedral in dunites. The compositions of Cr-spinels range from Cr-picotite to Cr-magnetite (Figure 7a) [25], showing elevated contents of divalent and trivalent iron (Table 5 and Table S5). The Cr-spinel composition varies from low-Cr varieties in peridotites (Cr# = 0.25–0.45) to high-Cr varieties in dunites and pyroxenites (Cr# = 0.6–0.7) (Figure 7b).

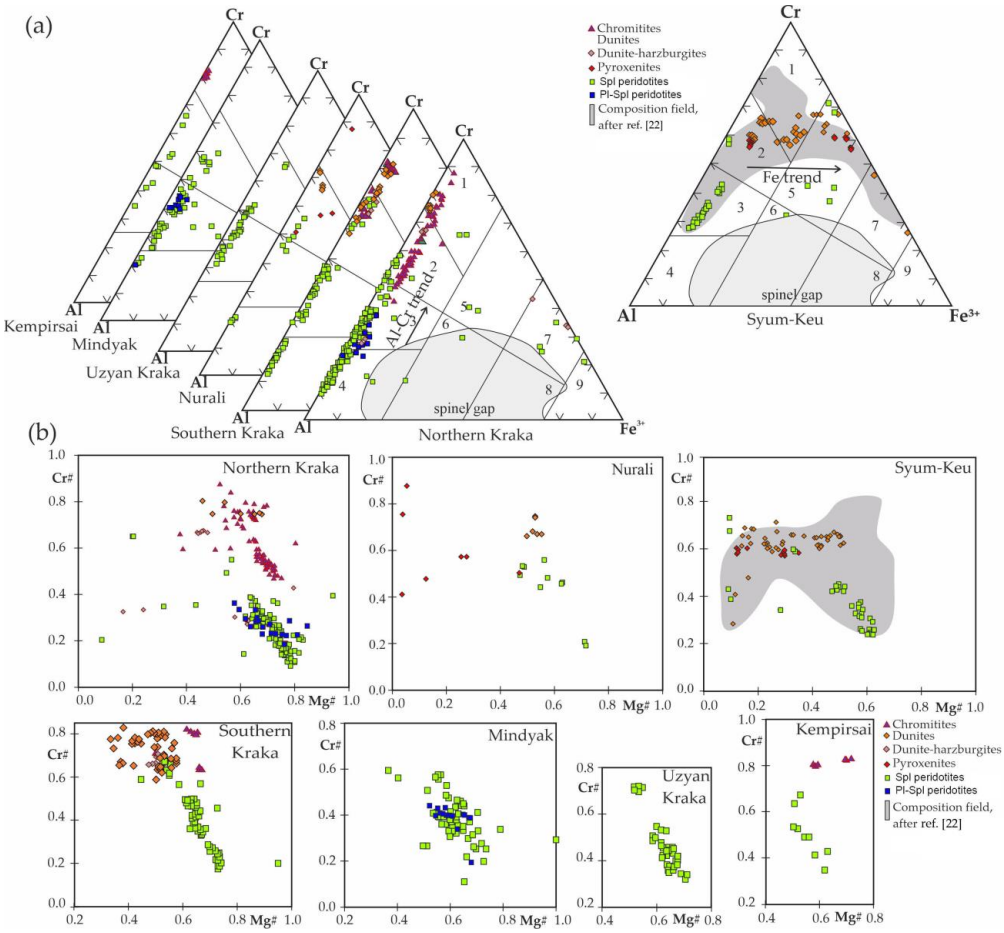

Figure 7. Comparison of compositions of Cr-spinel of Syum-Keu and ophiolitic massifs of the Southern Urals: (**a**) On the classification diagram, following [30]: 1—chromite, 2—Al-chromite, 3—Cr-picotite, 4—picotite (hercynite), 5—Fe-chromite, 6—Fe-picotite, 7—Cr-magnetite, 8—Al-magnetite, 9—magnetite. (**b**) On the Mg#–Cr# diagram: Cr# = Cr/(Cr + Al + Fe^{3+}), Mg# = Mg/(Mg + Fe^{2+}) [20,22,31–34]. "Spinel gap" field from [35].

Table 5. Representative analyses of Cr–spinel grains from ultramafic rocks of the Syum-Keu massif.

wt.%	1	2	3	4	5	6	7	8
MgO	7.2	2.9	2.2	8.3	13.0	12.39	12.4	4.2
FeO*	33.8	45.7	67.1	28.5	21.5	26.12	30.4	43.3
Al_2O_3	11.9	3.0	0.1	11.9	35.6	32.90	32.9	8.9
Cr_2O_3	47.2	45.5	25.6	50.4	29.7	26.57	26.6	42.7
TiO_2	0.4	1.0	1.2	0.4	bdl	0.08	0.1	1.1

Table 5. *Cont.*

wt.%	1	2	3	4	5	6	7	8
V_2O_3	0.2	0.5	bdl	bdl	0.3	0.13	0.1	0.3
MnO	0.5	0.5	0.8	0.6	0.1	0.29	0.3	0.6
Total	101.2	99.1	97.0	100.1	100.2	98.48	102.8	101.1
apfu								
Mg	0.35	0.16	0.12	0.41	0.55	0.52	0.48	0.21
Fe^3	0.29	0.51	1.19	0.20	0.09	0.31	0.12	0.45
Fe^2	0.63	0.82	0.84	0.58	0.44	0.44	0.50	0.76
Al	0.45	0.13	–	0.46	1.18	1.09	1.01	0.34
Cr	1.24	1.31	0.77	1.33	0.72	0.59	0.88	1.16
Ti	0.010	0.026	0.035	0.010	0.001	0.001	0.001	0.028
Mn	0.014	0.016	0.026	0.016	0.001	0.007	0.005	0.019
V	0.004	0.015	–	0.001	0.007	0.004	0.006	0.010
Cr#	0.62	0.67	0.39	0.67	0.36	0.30	0.44	0.59
Mg#	0.35	0.16	0.13	0.41	0.56	0.54	0.49	0.21

1–4—dunite, 5–7—harzburgite and lherzolite, 8—orthopyroxenite; bdl—below detection limit; Cr# = $Cr/(Fe^{3+} + Al + Cr)$; Mg# = $Mg/(Mg + Fe^{2+})$; FeO* = $FeO + Fe_2O_3$.

4.4. Mineralogy of Mafic Rocks

As noted above, the rock-forming minerals of mafic rocks are represented by plagioclase, pyroxenes, amphiboles, and garnet. In thin sections, plagioclase occurs as xenomorphic grains or laths, exhibiting low relief under parallel nicols with cleavage observed in one, and occasionally in two, directions. Anhedral grains can reach the size of up to 1.1 mm, while the laths are much smaller, measuring up to 0.10–0.15 mm. The plagioclase grains are characterized by an elevated CaO content (19.0–20.0 at.%) and chemically belong to anorthite, with one analysis falling into the oligoclase field (Figure 8; Table S6).

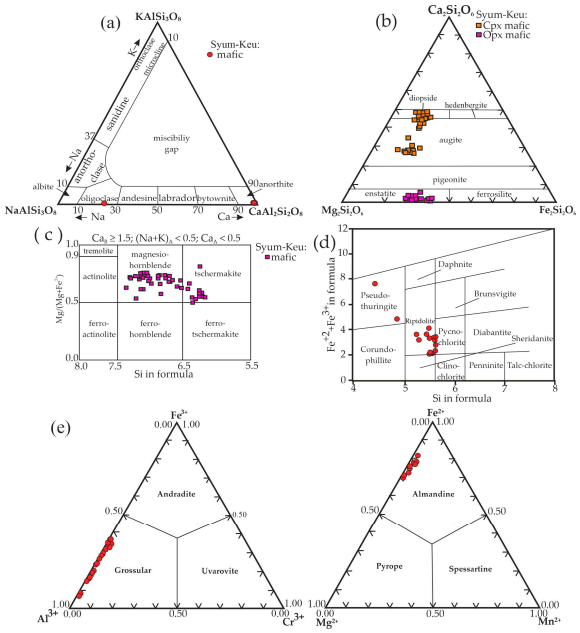

Figure 8. Features of rock–forming mineral compositions: (**a**)—plagioclases; (**b**)—pyroxenes; (**c**)—amphiboles, following [26]; (**d**)—chlorites, following [36]; (**e**)—garnets. Cpx—clinopyroxenes, Opx—orthopyroxenes.

Pyroxenes in thin sections also occur in anhedral grains 0.4–1.1 mm in size. Orthopyroxene is represented by a high-iron variety ($Fs_{35–40}$) known as hypersthene (Figure 8b; Table S2). Clinopyroxene is compositionally related to diopside and rarely to high-Fe augite ($Fs_{19–20}$). The amphiboles are classified as magnesian hornblende ($Ca_2[Mg_4(Al,Fe^{3+})]Si_7AlO_{22}(OH)_2$), tschermakite ($Ca_2(Mg_3AlFe^{3+})Si_6Al_2O_{22}(OH)_2$), and ferrotschermakite ($Ca_2(Fe^{2+}{}_3AlFe^{3+})Si_6Al_2O_{22}(OH)_2$) (Figure 8c; Table S3) [26]. The rocks also contain chlorites, compositionally corresponding to ripidolite, pycnochlorite, and pseudothuringite (Figure 8d; Table S7). In thin sections, garnets occur as segregations 0.4–0.8 mm in size, occasionally reaching 1 cm (S-318-1). Based on their composition, the garnets are classified as almandine ($Fe^{2+}{}_3Al_2[SiO_4]_3$) from the Prp-Alm-Sps series and grossular ($Ca_3Al_2[SiO_4]_3$) from the Uv-Grs-Adr series (Figure 8e; Table S8), which is consistent with the previously established characteristics of these rocks [21]. Of note, magnesian olivine grains (Fo_{88}) were found in gabbroids (sample S-313-2). Accessory minerals in gabbroids include ilmenite ($FeTiO_3$) (15–20 μm), pyrite (FeS_2) (0.4–0.5 μm), rutile (TiO_2), titanomagnetite (Fe_2TiO_4) (0.5 μm), and chalcopyrite ($CuFeS_2$) (Figure 6e,f; Table S9).

4.5. Microstructure of Ultramafic Rocks

We conducted a microstructural analysis of the freshest ultramafic rock samples from various parts of the upper mantle section of the massif. The most significant findings relate to the lattice preferred orientation (LPO) of olivine (Figure 9). The LPO diagrams show different types of olivine fabric. Most commonly, the lineation of the rock (L), defined by the elongation of olivine grains or Cr-spinel aggregates in the foliation plane (S), aligns with or forms a small angle relative to the [100] axis in olivine, while the other axes exhibit variable orientations with respect to S.

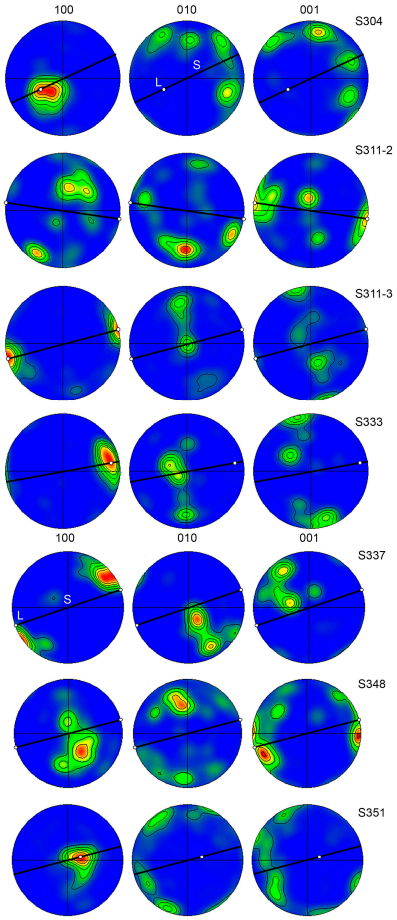

Figure 9. Olivine lattice preferred orientations (LPO) in Syum-Keu peridotites. The color coding refers to the density of data points. S—foliation, L—lineation.

In most cases, the [010] and [001] axes form girdles in a plane perpendicular to S, indicating a D-type olivine fabric. This texture was observed in peridotite samples S-304-1 and S-311-3, as well as in disseminated banded chromitite within dunite sample S-351. This D-type fabric is primarily formed by slip along the [100] axis, occurring across multiple planes in the {0kl} family.

In two peridotite samples (S-333, S-337), the [010] axis lies within the S plane, while [001] is perpendicular to it (Figure 9). This pattern characterizes the E-type fabric, which was also formed by slip along the [100] axis, with a prevalent slip plane of [001].

Finally, in two samples (S-311-2, S-348), a B-type olivine fabric was observed, where the [001] axis aligns with or forms a small angle to the lineation. In sample S-348, the orientation closest to S is marked by the [100] axis, indicating predominant slip along the (010)[001] system. In sample S-311-2, the pattern is similar, but exhibits secondary maxima, suggesting a more complex microstructure.

5. Discussion

5.1. Mineralogical and Geochemical Features of Ultramafic and Mafic Rocks

According to [19], the Syum-Keu massif, like other members of the Polar Ural group (e.g., Rai–Iz and Voikaro–Syninsky), belongs to supra-subduction ophiolite complexes formed in back-arc and inter-arc marginal basins in the Early and Middle Paleozoic. A comparison of Syum-Keu's ultramafic rocks with those of the Southern Ural ophiolite massifs highlights distinct mineralogical features. Thus, amphiboles found in the lherzolite units of Kraka (both Northern and Southern) and Syum-Keu indicate specific formation conditions of ultramafic rocks during their ascent from the upper mantle and subsequent metamorphism.

Amphiboles in the studied massifs primarily include tschermakite ($Ca_2(Mg_3AlFe^{3+})Si_6Al_2O_{22}(OH)_2$), magnesian hornblende ($Ca_2[Mg_4(Al,Fe^{3+})]Si_7AlO_{22}(OH)_2$), tremolite ($Ca_2Mg_5Si_8O_{22}(OH)_2$), pargasite ($NaCa_2(Mg_4Al)Si_6Al_2O_{22}(OH)_2$), and edenite ($NaCa_2Mg_5Si_7AlO_{22}(OH)_2$) (Figure 10a). In the $Al^{IV} - (Na + K)$ diagram, most of the Northern Kraka samples fall within the hornblende field (Figure 10b). In other massifs, the amphibole compositions shift toward the pargasite field. Discrimination diagrams separate the Syum-Keu peridotite amphiboles from those of the Kraka massif, placing them in the "metamorphic" field in one diagram (Figure 10c) and close to the boundary of "magmatic" and "metamorphic" amphiboles (Figure 10d) in another. Additionally, in the Al_2O_3–TiO_2 diagram, Syum-Keu amphibole compositions cluster within the "crust–mantle source" field, while Kraka amphiboles exhibit a wider compositional range of values with a trend toward the "mantle component".

Given that Cr-spinels prevail in the ultramafic rocks, display significant compositional variability, and show better resistance to serpentinization compared to rock-forming silicates, we conducted a comparative analysis of their chemistry to elucidate the formation conditions of massif rocks. Cr-spinels from the Syum-Keu ultramafic rocks differ chemically from those in the Southern Urals ophiolite massifs. In the Southern Urals massifs, the Cr-spinel points align along the Al-Cr trend on a ternary diagram, while the Syum-Keu Cr-spinels exhibit an Fe trend (Figure 7a). In the Syum-Keu peridotites, Cr-spinels form a trend where the magnesium content (Mg#) gently dips as the chromium content (Cr#) increases, similar to the South Ural massifs (Figure 7b). The Cr-spinels in dunites follow a subhorizontal trend, with values ranging from 0.6 to 0.65. The comparatively low Cr# and Mg# values compared to the Southern Urals are associated with an elevated Fe^{2+} and Fe^{3+} content.

In the geodynamic diagrams, Mg#–Cr#, Cr#-Fe^{3+}, Cr_2O_3—Al_2O_3, Cr#—$Fe^{3+}/(Fe^{3+} + Fe^{2+})$, and TiO_2-Cr# Cr-spinels from dunites and pyroxenites plot within the fields for fore-arc settings (e.g., Southern Sandwich Arc (SSF) and the Torishima Seamount (TS), Figure 11a–d). Meanwhile, points for harzburgites and lherzolites trend toward abyssal peridotite fields (Figure 11a,b). In the TiO_2-Cr# diagram, Cr-spinels from dunites and pyroxenites mainly lie between the rock reaction trends with boninite and island-arc tholeiitic melts (Figure 11e). Additionally, clinopyroxenes from ultramafic rocks were analyzed, falling into the fields of island arcs, mid-ocean ridge basalts, and boninites on the covariance diagram (Figure 11f).

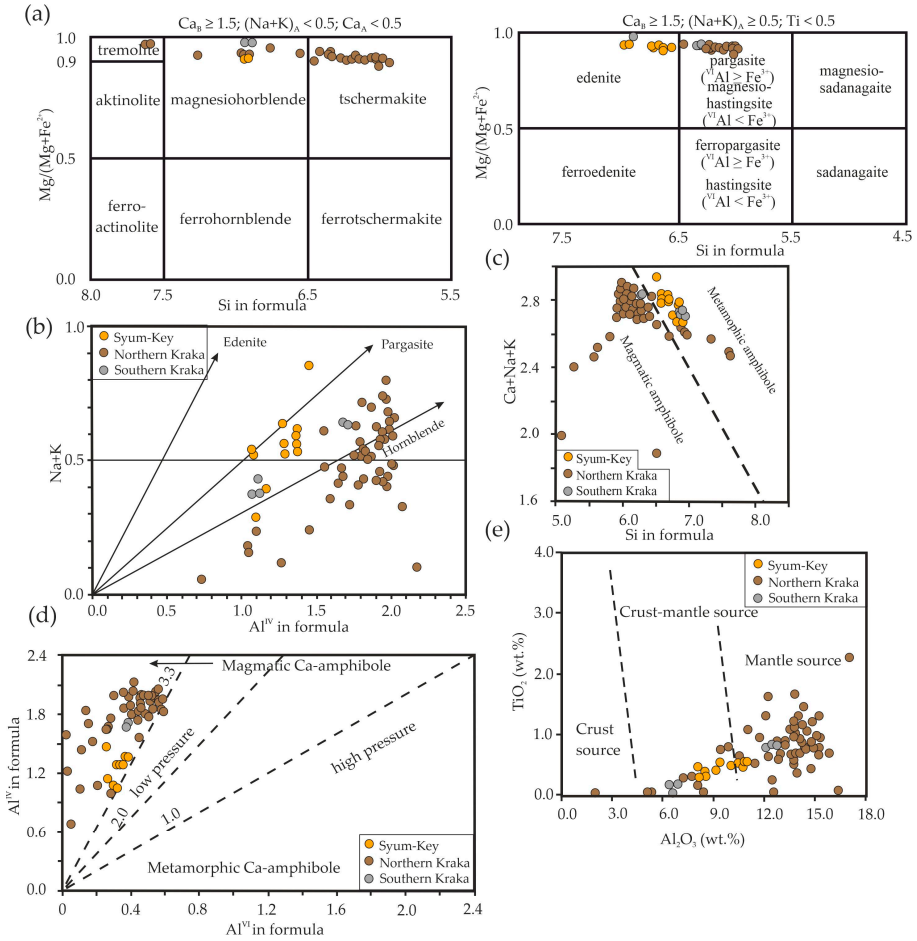

Figure 10. Composition of amphiboles: (**a**)—classification diagrams Si vs. $Mg/(Mg + Fe^{2+})$, after [26]; (**b**)—Al^{IV} a.p.f.u. vs. Na + K, following [37]; (**c**)—diagram Si vs. Ca + Na + K a.p.f.u., after [38]; (**d**)—diagram Al^{VI}–Al^{IV} a.p.f.u., following [39]; (**e**)—diagram Al_2O_3–TiO_2 in wt.%, following [40].

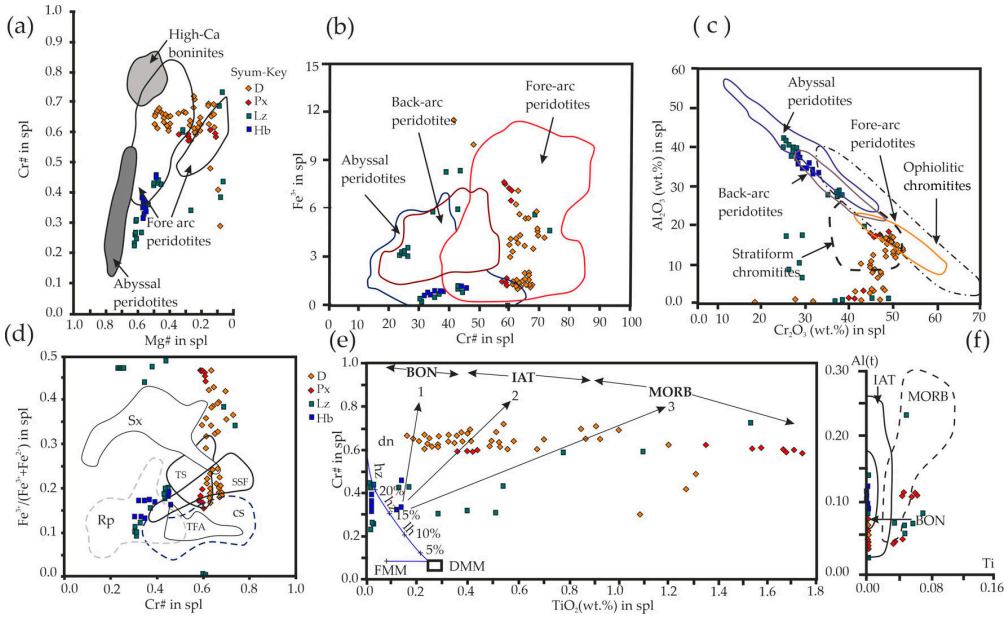

Figure 11. (**a**–**e**) Geodynamic diagrams: (**a**) Mg# vs. Cr# in Cr-spinel with fields of abyssal peridotites, boninites, after [3], and fore-arc after [5]; (**b**) Cr# vs. Fe^{3+} in Cr-spinel, after [8]; (**c**) Cr_2O_3 vs. Al_2O_3 in Cr-spinel, after [9]; (**d**) Cr# vs. $Fe^{3+}/(Fe^{3+}+Fe^{2+})$ Cr-spinel, after [7]. Fore-arc peridotites: SSF—South

Sandwich Arc, CS—Cone Seamount, TS—Torishima Seamount, TFA—Tonga Fore-arc; Sx—subduction xenoliths, Rp—ridge peridotites. (**e**) TiO_2 vs. Cr#, after [6], showing the degree of melting in mantle rocks (curve labeled 5.0%, 10.0%, 15.0%, and 20.0%). Response trends with boninite melts (1), island-arc tholeiitic melts (2), and MORB melts (3). (**f**) Ti vs. Al(t) in clinopyroxenes, IAT—island-arc tholeiites, BON—boninite, MORB—mid-ocean ridge basalts, after [4]. D—dunite; Hb—harzburgite; Lz—lherzolite; Px—pyroxenite.

5.2. Evaluation of P-T-fO_2 Conditions of Upper Mantle Section Formation

The degree of melting in the Syum-Keu peridotites evaluated using the OSMA diagram (Figure 12a) indicates that these rocks represent refractory residues from various degrees of partial melting of pyrolite (10%–30%). Lherzolites exhibit a narrower range of 10%–20%, falling into the field of abyssal and suprasubduction peridotites [41]. To evaluate the P–T conditions of peridotite formation, we used three types of olivine–Cr-spinel geothermometers and five types of two-pyroxene geothermometers. For the olivine–Cr-spinel pair, temperatures were estimated using three types of geothermometers, i.e., Fabries (GTF) [42], Roeder–Campbell–Jamieson (GTRCD) [43], and Ono (GTO) [44]. Results indicate equilibrium temperatures mainly in a range from 500 to 600 °C (with average values of 520 °C for GTO, 596 °C for GTF, and 859 °C for GTRCD) (Figure 12b). For two-pyroxene systems, geothermometers (Wood–Banno (GTWB) [45], Wells (GTW) [46], and Putirka (GTP) [47]) showed higher closure temperatures for the Fe-Mg exchange reaction, mostly falling within 700–900 °C (averaging 968 °C for GTWB, 820 °C –for GTP, and 838 °C for GTW) (Figure 12c).

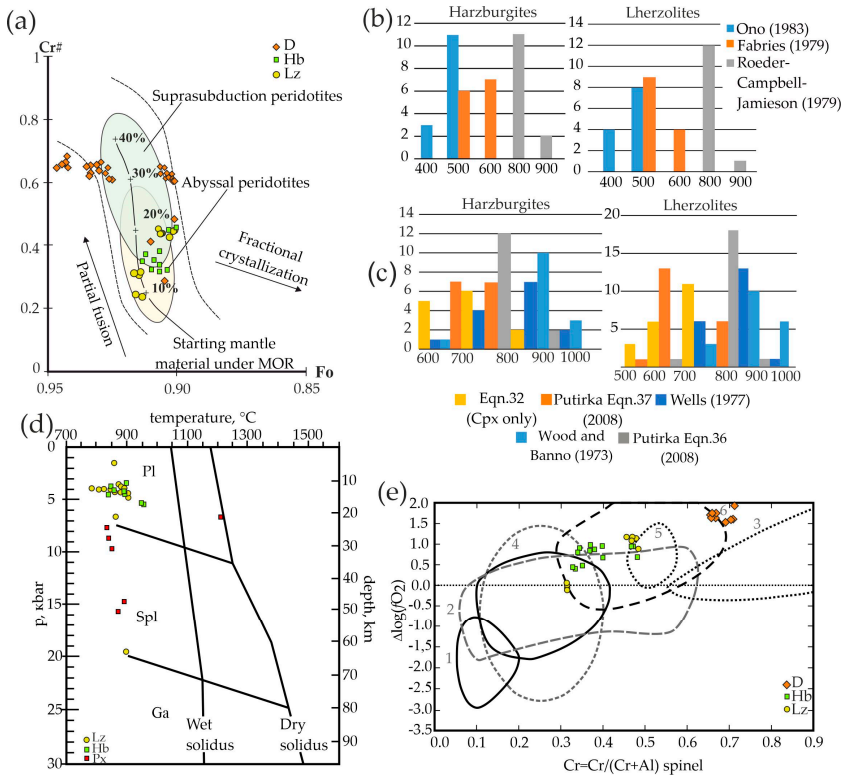

Figure 12. P–T conditions for the formation of mineral associations of ultramafic rocks. (**a**) OSMA diagram for coexisting olivine and Cr-spinel grains, after [41]; (**b**) distribution of equilibrium temperatures in olivine–Cr-spinel pairs for peridotites, after [42–44]; (**c**) distribution of equilibrium temperatures in diopside–enstatite pairs for peridotites, after [45–47]; (**d**) P–T conditions of mantle peridotites, with fields based on data following [47–49]; (**e**) Cr# vs. $\Delta \log fO_2$ diagram: margins based on data following [50,51] (1–3—peridotite xenoliths (1—primitive, 2—weakly metasomatised, 3—intensely metasomatised), 4–5—abyssal peridotites, 6—suprasubduction peridotites; bold lines outline the fields of abyssal peridotites and peridotites of island arcs; D—dunite; Hb—harzburgite; Lz—lherzolite; Px—pyroxenite.

The temperatures of two-pyroxene geothermometers are 150–200 °C higher than those from the olivine–Cr-spinel geothermometers. Such a discrepancy is typical of ophiolitic ultramafic rocks and xenoliths, as noted by numerous researchers [52,53]. This difference is explained by contrasting diffusion rates of Fe^{2+} and Mg^{2+} cations in these mineral pairs. Equilibrium is achieved most rapidly between pyroxenes, while in olivine–Cr-spinel pairs, this process occurs over a longer timescale and ceases at lower temperatures. The pressure conditions for spinel peridotite associations can be estimated using the GBP pyroxene geobarometer [47] (Figure 12d) at 4–5 kbar (occasionally up to 20 kbar), corresponding to a depth of 11–15 km. Redox conditions during mineral formation in the upper mantle were evaluated using an oxybarometer [50] based on the composition of coexisting olivine and spinel grains. The obtained data range from −0.25. . . to +1.8 $\Delta \log fO_2$ (FMQ) (Figure 12e).

Our conclusions generally corroborate the ideas introduced by former researchers [19,54] regarding a longer evolution of the upper mantle ultramafic rocks of the Syum-Keu massif compared to those of the Kraka massif. Of not, the comparison of mineral equilibrium temperatures of olivine–spinel and two-pyroxene pairs in the Syum-Keu and Southern Ural massifs shows that the latter exhibit values 200–300 °C higher. There is a difference in the distribution of points on the Cr# vs. $\Delta \log fO_2$ diagram, where values for the Syum-Keu massif fall within the field of suprasubduction peridotites, while those for the Southern Ural ophiolites occur in the abyssal field.

5.3. Microstructural Evolution of the Mantle Section

LPO of rock-forming minerals in ultramafic rocks is typically interpreted as evidence of plastic flow in the dislocation creep regime in the upper mantle [55–57]. It is also widely discussed in the literature that fabric types of olivine and some other minerals can provide insights into external parameters (P, T, and H_2O content) [58,59]. As noted above, D-type prevails in peridotites, while B-type and E-type are minor.

Our results are generally consistent with earlier microstructural studies conducted on a universal stage [16]. The latter study also reported the widespread occurrence of D-type olivine fabric in peridotites. Additionally, the researcher noted that the relationship between the macrostructure and olivine LPO changes as the volume fraction of neoblasts increases in the rock, indicating a transition from protogranular to mosaic textures. In protogranular and porphyroclastic olivines, [100] coincides with or forms a small angle with lineation, forming an intense single maximum. In samples with a high fraction of neoblasts, the [100] maximum shows dispersion and deviates significantly from the lineation, the [001] axis often being the closest to it [16]. Our studies also corroborate these observations. The observed changes in the olivine LPO are likely to reflect a transition from relatively high-temperature slip along the {0kl}[100] system to lower-temperature slip along the {110}[001] system, accompanied by widespread recrystallization. This was also previously proposed in [16]. The observed patterns may suggest changing the plastic flow conditions of the Syum-Keu ultramafic rocks as they ascended from the upper mantle to the lower crust.

In addition to statistical LPO data for olivine, we constructed microstructural maps showing grain boundaries classified into high-angle and low-angle boundaries (LAGBs), the latter also known as sub-grain boundaries. Unlike typical maps of upper mantle tectonites, Figure 13 shows no linear LAGBs, which usually correspond to kink-band boundaries and are diagnosed in rocks deformed under upper mantle conditions. In this case, the LAGB structure is mosaic (equilibrium) in nature. It can be interpreted as a result of post-deformation annealing (polygonization?), which may have occurred as the massif was forming at the lower crustal depths.

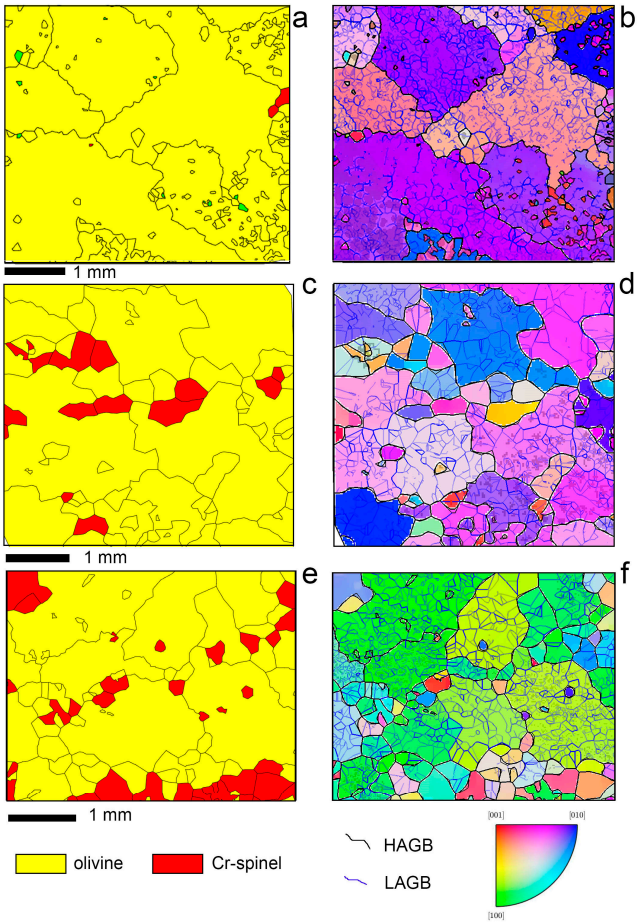

Figure 13. Phase composition maps (**a**,**c**,**e**) and microstructural maps in the encoding of inverse pole figures (**b**,**d**,**f**) for some samples of Syum–Keu peridotites. HAGB—high-angle grain boundaries, LAGB—low-angle grain boundaries (sub-boundaries). Data processing was carried out in the MTEX program [60,61].

6. Conclusions

Our studies of the mineralogy, geochemistry, and microstructure of the ultramafic and mafic rocks in the Syum-Keu massif expanded and refined existing knowledge in this area, shedding light on the petrological evolution of the matter in the upper mantle and mafic melts during the formation of the ophiolite complex. While the ultramafic rocks of the massif are mineralogically and compositionally close to the lherzolite type, some of their compositional and structural features set them apart from similar massifs in the Southern Urals:

1. In particular, compositions of accessory Cr-spinel grains and amphiboles of the Syum-Keu and Kraka massifs differ significantly. Cr-spinel grains in the Syum-Keu ultramafic rocks show elevated iron content and a pronounced Fe trend, indicating intense crustal metamorphism.
2. Similarly, amphiboles in the Syum-Keu ultramafic rocks exhibit a significant proportion of the crustal (metamorphic) component, while the same minerals in the Kraka massif suggest a mantle (magmatic) origin. A high degree of metamorphism is also typical of the mafic rocks of the Syum-Keu massif.
3. The microstructure of olivine from the Syum-Keu peridotites reflects two stages of the plastic flow: early (upper mantle) and late (lower crustal). The first stage corresponds to a higher-temperature flow along the {0kl}[100] system, and the second stage aligns with a lower-temperature flow along the {110}[001] system.
4. Finally, two-pyroxene geothermobarometry revealed that the formation conditions of the massifs have some differences, i.e., the Southern Urals massifs display higher

temperatures and pressures at the spinel-plagioclase facies boundary of the upper mantle, while the Syum-Keu ultramafic rocks show lower values that likely indicate their formation in the lower crust.

Supplementary Materials: The following supporting information can be downloaded at: https://www.mdpi.com/article/10.3390/min14121245/s1, Table S1: Composition of olivine grains; Table S2: Composition of pyroxene grains; Table S3: Composition of amphibole grains; Table S4: Composition of PGMs; Table S5: Composition of Cr-spinel grains; Table S6: Composition of plagioclase grains; Table S7: Composition of chlorites; Table S8: Composition of garnet grains; Table S9: Composition of BMS grains.

Author Contributions: Conceptualization, methodology, writing, D.E.S.; investigation, field work, sample preparation, T.D.S., D.E.S., A.A.S., and R.A.G., writing—original draft preparation, T.D.S.; writing—review and editing, D.E.S. and R.A.G.; visualization, T.D.S., D.E.S., and A.A.S.; project administration, funding acquisition, D.E.S. All authors have read and agreed to the published version of the manuscript.

Funding: This study is supported by the Russian Science Foundation grant no. 22-17-00019 (https://rscf.ru/project/22-17-00019/, accessed on 11 May 2022).

Data Availability Statement: The data presented in this study are available on request from the corresponding author.

Acknowledgments: The authors are very grateful to T. A. Miroshnichenko for editing the English language of this manuscript, three reviewers for the useful comments that allowed to significantly improve the manuscript, and I. I. Musabirov for the EBSD study of ultramafic rocks.

Conflicts of Interest: The authors declare no conflicts of interest.

References

1. Ringwood, A.E. *Composition and Structure of the Earth's Mantle*; McGraw-Hill: New York, NY, USA, 1975; p. 618.
2. Coleman, R.G. *Ophiolites: Ancient Oceanic Lithosphere? (Minerals and Rocks)*; Springer: Berlin/Heidelberg, Germany; New York, NY, USA, 1977; Volume 12, p. 229. [CrossRef]
3. Dick, H.J.B.; Bullen, T. Chromian spinel as a petrogenetic indicator in abyssal and alpine type peridotites and spatially associated lavas. *Contrib. Mineral. Petrol* **1984**, *86*, 54–76. [CrossRef]
4. Beccaluva, L.; Macciotta, G.; Piccardo, G.B.; Zeda, O. Clinopyroxene composition of ophiolite basalts as petrogenetic indicator. *Chem. Geol* **1989**, *77*, 165–182. [CrossRef]
5. Ishii, T.; Robinson, P.T.; Maekawa, H.; Fiske, R. Petrological studies of peridotites from diapiric serpentinite seamounts in the Isu–Ogasawara–Mariana forearc, Leg 125. *Proc. Ocean Drill. Prog Sci. Results* **1992**, *125*, 445–485. [CrossRef]
6. Pearce, J.A.; Barker, P.P.; Edwards, S.J.; Parkinson, I.J.; Lear, P.T. Geochemistry and tectonic significance of peridotites from the South Sandwich arc-basin system, South Atlantic. *Contrib. Mineral. Petrol.* **2000**, *139*, 36–53. [CrossRef]
7. Parkinson, I.J.; Arculus, R.J.; Eggins, S.M. Peridotite xenoliths from Grenada, Lesser Antilles Island Arc. *Contrib. Mineral. Petrol.* **2003**, *146*, 241–262. [CrossRef]
8. Lian, D.; Yang, J.; Robinson, P.T.; Liu, F.; Xiong, F.; Zhang, L.; Gao, J.; Wu, W. Tectonic evolution of the western Yarlung Zangbo Ophiolitic Belt, Tibet: Implications from the petrology, mineralogy, and geochemistry of peridotites. *J. Geol.* **2016**, *124*, 353–376. [CrossRef]
9. Farré-de-Pablo, J.; Pujol-Solà, N.; Torres Herrera, H.; Aiglsperger, T.; González, J.M.; Llanes-Castro, A.I.; Garcia-Casco, A.; Proenza, J.A. Orthopyroxenite hosted chromitite veins anomalously enriched in platinum-group minerals from the Havana-Matanza Ophiolite, Cuba. *Boletín Soc. Geol. Mex.* **2020**, *72*, A110620. [CrossRef]
10. Akizawa, N.; Arai, S.; Tamura, A. Behavior of MORB magmas at uppermost mantle beneath a fast-spreading axis: An example from Wadi Fizh of the northern Oman ophiolite. *Contrib. Mineral. Petrol.* **2012**, *164*, 601–625. [CrossRef]
11. Abdel-Karim, A.-A.M.; El-Shafei, S.A. Mineralogy and chemical aspects of some ophiolitic metaultramafics, central Eastern Desert, Egypt: Evidences from chromites, sulphides and gangues. *Geol. J.* **2018**, *53*, 580–599. [CrossRef]
12. Ovung, T.N.; Ray, J.; Ghosh, B.; Koeberl, C.; Topa, D.; Paul, M. Clinopyroxene composition of volcanics from the Manipur Ophiolite, Northeastern India: Implications to geodynamic setting. *Int. J. Earth Sci.* **2018**, *107*, 1215–1229. [CrossRef]
13. Yang, Y.; Yang, J.; Wu, W.; Cai, P.; Ma, H. Microstructural Insights into the Evolution of Ophiolitic Chromite from Luobusha. *Minerals* **2023**, *13*, 1047. [CrossRef]
14. Xiong, Q.; Henry, H.; Griffin, W.L.; Zheng, J.-P.; Satsukawa, T.; Pearson, N.J.; O'Reilly, S.Y. High-and low-Cr chromitite and dunite in a Tibetan ophiolite: Evolution from mature subduction system to incipient forearc in the Neo-Tethyan Ocean. *Contrib. Mineral. Petrol.* **2017**, *172*, 45. [CrossRef]

15. Zucali, M.; Spalla, M.I.; Gosso, G. Multiscalar structural study of the ultramafic rocks of the Antrona Ophiolite (Pennine Alps). *J. Virtual Explor.* **2012**, *41*, 4. [CrossRef]
16. Shmelev, V.R. *Ultrabasites of the Syum-Keu Massif (Arctic Urals): Structure, Petrology, and Dynamometamorphism*; IGiG UrO AN SSSR: Yekaterinburg, Russia, 1991; p. 79. (In Russian)
17. Ponomareva, T.A.; Pystin, A.M. Structural features of the Marunkeu eclogite-gneiss complex of the Polar Urals based on gravimagnetic data. *Bull. IG Komi Sci. Cent. Ural. Branch Russ. Acad. Sci.* **2019**, *2*, 14–21. (In Russian) [CrossRef]
18. Perevozchikov, B.V.; Plotnikov, A.V.; Makiev, T.T. The nature of variations in the composition of ore and accessory chrome spinel of the ultramafic massif SyumKeu (Polar Urals). *News Univ. Geol. Explor.* **2007**, *4*, 32–39. (In Russian)
19. Puchkov, V.N. *Geology of the Urals and the Cis-Urals (Current Issues of Stratigraphy, Tectonics, Geodynamics and Metallogeny)*; DesignPoligraf Service: Ufa, Russia, 2010; p. 280. (In Russian)
20. Gurskaya, L.I.; Smelova, L.V.; Kolbantsev, L.R.; Lyakhnitskaya, V.D.; Lyakhnitsky, Y.S.; Shakhova, S.N. *Platinum Group Metals of Chromite-Bearing Massifs of the Polar Urals*; Publishing House of the St. Petersburg Map Factory of VSEGEI: St. Petersburg, Russia, 2004; p. 306. (In Russian)
21. Dobretsov, N.L.; Moldavantsev, Y.E.; Kazak, A.P.; Ponomareva, L.G.; Savelyeva, G.N.; Savelyev, A.A. *Petrology and Metamorphism of Ancient Ophiolites*; Science: Novosibirsk, Russia, 1977; p. 220. (In Russian)
22. Makeev, A.B.; Brianchaninova, N.I. *Topomineralogy of Ultrabasites of the Polar Urals*; Nauka: St. Petersburg, Russia, 1999; p. 252. (In Russian)
23. Savelieva, G.N.; Suslov, P.V. Structure and composition of mantle peridotites at the boundary with crustal complexes of ophiolites in the Syum-Keu massif, Polar Urals. *Geotectonics* **2014**, *48*, 347–358. [CrossRef]
24. Savelieva, G.N.; Batanova, V.G.; Sobolev, A.V. Pyroxene–Cr-spinel exsolution in mantle lherzolites of the Syum-Keu ophiolite massif (Arctic Urals). *Russ. Geol. Geophys.* **2016**, *57*, 1419–1436. [CrossRef]
25. Perevozchikov, B.V.; Bulykin, L.D.; Popov, I.I.; Orfanitsky, V.L.; Andreev, M.I.; Snachev, V.I.; Danilenko, S.A.; Cherkasov, V.L.; Chentsov, A.M.; Zharikova, L.N.; et al. *Register of Chromite Occurrences in Alpine-Type Hyperbasitic Rocks of the Urals*; KamNIIKIGS: Perm, Russia, 2000; p. 474. (In Russian)
26. Leake, B.E.; Woolley, A.R.; Arps, C.E.S.; Birch, W.D.; Gilbert, M.C.; Grice, J.D.; Hawthorne, W.C.; Kato, A.; Kisch, K.J.; Krivovichev, V.G.; et al. Nomenclature of amphiboles; report of the subcommittee on amphiboles of the International Mineralogical Association commission on new minerals and mineral names. *Can. Mineral.* **1997**, *35*, 219–246. [CrossRef]
27. Whitney, D.L.; Evans, B.W. Abbreviations for names of rock-forming minerals. *Am. Mineral.* **2010**, *95*, 185–187. [CrossRef]
28. Dmitriev, L.V.; Ukhanov, A.V.; Sharaskin, L.Y. On the composition of the upper mantle. *Geochemistry* **1972**, *10*, 1155–1167. (In Russian)
29. Middlemost, E.A.K. Naming materials in the magma, igneous rock system. *Earth Sci. Rev.* **1994**, *37*, 215–224. [CrossRef]
30. Deer, W.A.; Howie, R.A.; Zussman, J. *An Introduction to the Rock-Forming Minerals*, 3rd ed.; Longman Scientific & Technical: Harlow, UK, 1992; p. 695.
31. Saveliev, D.E.; Gataullin, R.A. Lherzolites of the Aznagulovskaya area: Composition and P-T-fO2 formation conditions. *Her. Acad. Sci. Repub. Bashkortostan* **2021**, *40*, 15–25. (In Russian) [CrossRef]
32. Saveliev, D.E.; Gataullin, R.A.; Gaifullin, R.Y. Mineralogical and geochemical features and formation conditions of ultramafites of the Mindyak massif (Southern Urals). *Her. Acad. Sci. Repub. Bashkortostan* **2022**, *42*, 47–57. (In Russian) [CrossRef]
33. Gataullin, R.A.; Saveliev, D.E. Mineralogical and geochemical features of mantle ultramafites of the southern part of the Nurali massif. *Geol. Bull.* **2021**, *1*, 55–67. (In Russian) [CrossRef]
34. Saveliev, D.E.; Shilovskikh, V.V.; Makatov, D.K.; Gataullin, R.A. Accessory Cr-spinel from peridotite massifs of the South Urals: Morphology, composition and origin. *Mineral. Petrol.* **2022**, *116*, 401–427. [CrossRef]
35. Barnes, S.J.; Roeder, P.L. The range of spinel compositions in terrestrial mafic and ultramafic rocks. *J. Petrol.* **2001**, *12*, 2279–2302. [CrossRef]
36. Hey, M.H. A new review of the chlorites. *Min. Mag.* **1954**, *30*, 277–292. [CrossRef]
37. Kamali, A.A.; Moayyed, M.; Amel, N.; Mohammad, F.; Brenna, M.; Saumur, B.M.; Santos, J.F. Mineralogy, mineral chemistry and thermobarometry of postmineralization dykes of the Sungun Cu–Mo porphyry deposit (Northwest Iran). *Open Geosci.* **2020**, *12*, 764–790. [CrossRef]
38. Czamanske, G.K.; Wones, D.R. Oxidation during magmatic differentiation, Finnmarks Complex, Oslo Area, Norway: Part 2, the mafic silicate. *J. Petrol.* **1973**, *14*, 349–380. [CrossRef]
39. Ernst, W.G.; Liu, J. Experimental Phase-Equilibrium Study of Al-and Ti-contents of Calcic Amphibole in MORB—A Semiquantitative Thermobarometer. *Am. Mineral.* **1998**, *83*, 952–969. [CrossRef]
40. Changyi, J.; Sanyuan, A. On chemical characteristics of calcic amphiboles from igneous rocks and their petrogenesis significance. *J. Mineral. Petrol.* **1984**, *3*, 1–9.
41. Arai, S. Characterization of spinel peridotites by olivine-spinel compositional relationships: Review and interpretation. *Chem. Geol.* **1994**, *113*, 191–204. [CrossRef]
42. Fabries, J. Spinel-olivine geothermometry in peridotites from ultramafic complexes. *Contrib. Mineral. Petrol.* **1979**, *69*, 329–336. [CrossRef]
43. Roeder, P.L.; Campbell, I.H.; Jamieson, H.E. A re-evaluation of the olivine-spinel geothermometer. *Contrib. Mineral. Petrol.* **1979**, *68*, 325–334. [CrossRef]
44. Ono, A. Fe-Mg partioning between spinel and olivine. *J. Jpn. Assoc. Mineral. Petrol. Econ. Geol.* **1983**, *78*, 115–122. [CrossRef]

45. Wood, B.J.; Banno, S. Garnet-orthopyroxene and orthopyroxene-clinopyroxene relationships in simple and complex systems. *Contrib. Mineral. Petrol.* **1973**, *42*, 109–124. [CrossRef]
46. Wells, P.R.A. Pyroxene thermometry in simple and complex systems. *Contrib. Mineral. Petrol.* **1977**, *62*, 129–139. [CrossRef]
47. Putirka, K.D. Thermometers and barometers for volcanic systems. *Rev. Mineral. Geochem.* **2008**, *69*, 61–120. [CrossRef]
48. Green, D.H.; Falloon, T.J. Pyrolite: A Ringwood concept and its current expression. In *The Earth's Mantle Composition, Structure and Evolution*; Cambridge University Press: Cambridge, UK, 1998; Volume 3, pp. 311–378.
49. Ahmed, A.H.; Moghazi, A.K.M.; Moufti, M.R.; Dawood, Y.H.; Ali, K.A. Nature of the lithospheric mantle beneath the Arabian Shield and genesis of Al-spinel micropods: Evidence from the mantle xenoliths of Harrat Kishb, Western Saudi Arabia. *Lithos* **2016**, *240–243*, 119–139. [CrossRef]
50. Ballhaus, C.; Berry, R.F.; Green, D.H. High pressure experimental calibration of the olivine-orthopyroxene-spinel oxygen geobarometer: Implications for the oxidation state of the upper mantle. *Contrib. Mineral. Petrol.* **1991**, *107*, 27–40. [CrossRef]
51. Parkinson, I.J.; Pearce, J.A. Peridotites from the Izu-Bonin–Mariana forearc (ODP Leg 125): Evidence for mantle melting and melt–mantle interaction in a supra-subduction zone setting. *J. Petrol.* **1998**, *39*, 1577–1618. [CrossRef]
52. Ozawa, K. Evaluation of olivine-spinel geothermometry as an indicator of thermal history for peridotites. *Contrib. Mineral. Petrol.* **1983**, *82*, 52–65. [CrossRef]
53. Bazylev, B.A. Petrological and Geochemical Evolution of Mantle Matter in the Lithosphere: Comparative Study of Oceanic and Alpine-Type Spinel Peridotites. Ph.D. Thesis, Doctor of Geological and Mineral Sciences, GEOKHI, Moscow, Russia, 2003; p. 371.
54. Savelieva, G.N. *Gabbro–Ultrabasitic Complexes of the Urals Ophiolites and Their Analogs in the Recent Oceanic Crust*; Nauka: Moscow, Russia, 1987; p. 245. (In Russian)
55. Nicolas, A.; Bouchez, J.L.; Boudier, F.; Mercier, J.C. Textures, structures and fabrics due to solid state flow in some European lherzolites. *Tectonophysics* **1971**, *12*, 55–86. [CrossRef]
56. Carter, N.L. Steady state flow of rocks. *Rev. Geophys. Space Phys.* **1976**, *14*, 301–360. [CrossRef]
57. Karato, S.-I. *Deformation of Earth Materials. An Introduction to the Rheology of Solid Earth*; Cambridge University Press: New York, NY, USA, 2008; p. 463. [CrossRef]
58. Karato, S.-I.; Jung, H.; Katayama, I.; Skemer, P. Geodynamic significance of seismic anisotropy of the upper mantle: New insights from laboratory studies. *Annu. Rev. Earth Planet. Sci.* **2008**, *36*, 59–95. [CrossRef]
59. Jung, H. Crystal preferred orientations of olivine, orthopyroxene, serpentine, chlorite, and amphibole, and implications for seismic anisotropy in subduction zones: A review. *Geosci. J.* **2017**, *21*, 985–1011. [CrossRef]
60. Bachmann, F.; Hielscher, R.; Schaeben, H. Texture analysis with MTEX-Free and open source software toolbox. *Solid State Phenom.* **2010**, *160*, 63–68. [CrossRef]
61. Hielscher, R.; Silbermann, C.; Schmidl, E.; Ihlemann, J. Denoising of Crystal Orientation Maps. *J. Appl. Crystallogr.* **2019**, *52*, 984–996. [CrossRef]

Disclaimer/Publisher's Note: The statements, opinions and data contained in all publications are solely those of the individual author(s) and contributor(s) and not of MDPI and/or the editor(s). MDPI and/or the editor(s) disclaim responsibility for any injury to people or property resulting from any ideas, methods, instructions or products referred to in the content.